



# Microstructure Twinning and Mechanical Properties of Laser Melted Cu-10Sn Alloy for High Strength and Plasticity

Peng Yang, Xingye Guo, Dingyong He, Wei Shao, Zhen Tan, Hanguang Fu, Zhenlu Zhou, and Xiaoya Zhang

Submitted: 4 June 2021 / Revised: 15 September 2021 / Accepted: 16 October 2021 / Published online: 17 November 2021

A dense Cu-10Sn alloy bulk specimen was obtained by optimizing the laser powder bed fusion (L-PBF) processing, and the relative density of the specimen reached 99.7%. The grain morphology was mainly the columnar dendrite and inter-dendritic phases generated along the solidification direction. Tensile testing and detailed microstructural characterization were carried out on specimens in the as-built and heat-treated condition. Under the quasi-static tensile condition, the yield strength ( $\sigma_{0.2}$ ), ultimate tensile strength (UTS), and the elongation of the as-built Cu-10Sn specimen were 392 MPa, 749 MPa and 29%, respectively. After the solution treatment at 800 °C for 4 h, and aging treatment at 400 °C for 2 hours, the microstructure of the specimen transformed from the columnar grain to equiaxed grain, the dislocation density decrease, and numerous annealing twins were observed in the heat-treated state. Therefore, the quasi-static tensile yield strength ( $\sigma_{0.2}$ ) of the specimen was reduced to 245 MPa. However, the UTS and the elongation were increased to 840 MPa and 56%, respectively, due to the interaction between annealing twins and equiaxed grain.

**Keywords** Cu-10Sn alloy, heat treatment, laser powder bed fusion, mechanical properties

## 1. Introduction

Cu-Sn alloy has excellent mechanical properties, high wear resistance, great corrosion resistance, high electricity conductivity and good weld-ability (Ref 1, 2). It is widely used in the manufacturing industry of electrical and mechanical facility such as electrical connectors, high-precision springs and bearings. Currently, the demand for high-quality Cu-Sn alloy parts with complex structure and high mechanical properties is increasing with the rapid development of these industry fields. However, there are some drawbacks in the Cu-Sn alloy parts produced by traditional casting technology, such as large grain size, shrinkage cavity and pores, the low solubility in the solid solution phase and serious grain boundary segregation. The mechanical properties of the alloy may decrease due to the above factors (Ref 3). Compared with traditional casting technology, the novel-developed additive manufacturing technology can fabricate parts with complex structures with improved microstructure and mechanical properties, avoiding the defects introduced by casting technology.

The laser powder bed fusion (L-PBF) is one of the most studied additive manufacturing techniques based on powder bed fusion technology that produces metallic components with high relative density layer by layer using the laser as the input heat resource. According to this unique fabrication process, the L-PBF technology is preferable to manufacture components with very complex structure (Ref 4–6). The L-PBF technology has been widely recognized as a rapid prototyping technique with a delicate microstructure due to the high cooling speed, which might also generate the non-equilibrium solidification process. As a result of all the above mechanisms, it gives the unique characteristic in the microstructures, phase, chemical composition and mechanical properties (Ref 7, 8).

At present, some of the fabrication processes of Cu-Sn alloy using L-PBF technology have been studied (Ref 9–12). When the content of Sn increased to 10 wt.%, the powder could be fully melted, and the Cu-10Sn alloy specimens with relative density up to 99.7% were successfully prepared using L-PBF technology (Ref 13). Although it has some advantages over traditional methods, this new production method must overcome some problems including the high surface roughness, poor ductility, dimensional deviation, and formation of residual stresses in the processed parts (Ref 14). The appropriate heat treatment process, such as annealing and recrystallization, can eliminate the stress concentration and improve the plasticity (Ref 15–17). Mao *et al.* (Ref 18) investigate the manufacturing process and mechanical properties of high-tin bronze using the L-PBF technology, and the mechanical properties of the annealed L-PBF formed specimen were also studied. But there is no connection between the microstructure and mechanical properties. Tan *et al.* (Ref 19) build the Cu-alloy lattice structure using the L-PBF technology and evaluated the relationship between the heat transfer mechanism and the quality of the lattice structure. Ventura Li *et al.* (Ref 20) investigated the influence of the solution and artificial aging

Peng Yang, Xingye Guo, Wei Shao, Zhen Tan, Hanguang Fu, Zhenlu Zhou, and Xiaoya Zhang, Faculty of Materials and Manufacturing, Beijing University of Technology, Beijing 100124, People's Republic of China; and Dingyong He, Faculty of Materials and Manufacturing, Beijing University of Technology, Beijing 100124, People's Republic of China; and Beijing Engineering Research Center of Eco-materials and LCA, Beijing 100124, People's Republic of China. Contact e-mail: dyhe@bjut.edu.cn.

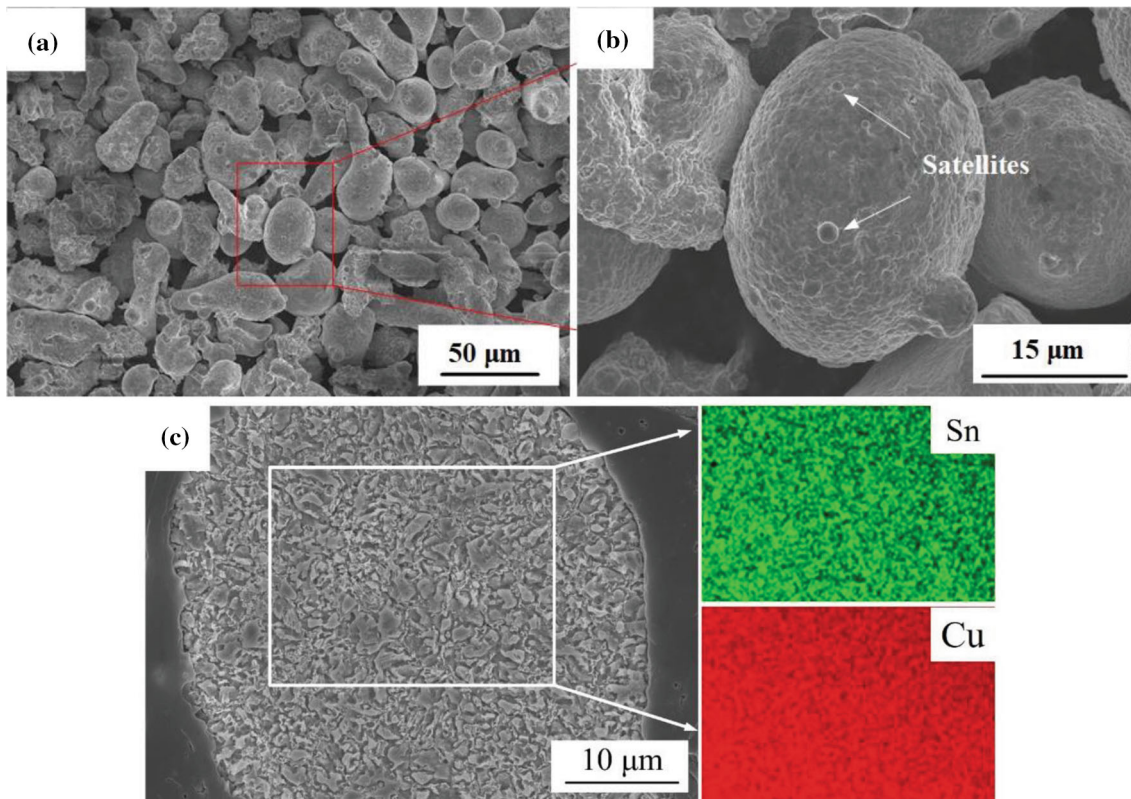


**Fig. 1** SEM microstructure images (Secondary electron image) of water atomized Cu-10Sn alloy powder: (a) x500; (b) x1500; (c) EDS images

treatments on the microstructures and mechanical properties of the as-built Cu-4.3Sn alloy parts.

In this work, a systematic investigation has been conducted on the influence of heat treatment on the microstructure and mechanical properties of L-PBF-produced Cu-10Sn alloy parts. To improve the mechanical properties of the as-built specimens, three types of heat treatment processes were designed according to the Cu-Sn phase diagrams, which are annealing, solution plus aging, and recrystallization. The objectives of this research are the investigation of the relations between the microstructural and mechanical properties of the as-built Cu-10Sn specimens with different heat treatment.

## 2. Experimental

### 2.1 Powders Characterization

The Cu-10Sn powder used in this work was prepared by the water atomization method. The chemical composition of the powder was analyzed by energy-dispersive x-ray spectrum (EDS) analysis. The EDS results indicated that the chemical composition of the powder was Cu 88.93 wt. % and Sn 11.07 wt. %. The initial morphology of Cu-10Sn powder was observed by scanning electron microscope (SEM), as shown in Figure 1. Although the morphology of powders prepared by water atomization was not exactly uniform, the majority of them had a spherical shape. As shown in the zoomed-in view of powders in Figure 1(b), some satellite particles adhered to the powder surface. In addition, the powder was uniform composition as shown in Figure 1(c) from the EDS images. The particle size of Cu-10Sn alloy powder was measured through

Tod Laser Particle Sizer. The particle size distribution was in the range of 15-63  $\mu\text{m}$  with an average size of 36  $\mu\text{m}$ . The flowability of the powder measured by Hall velocimeter was 21s for 50 g powder, and the apparent density of the powder was 2.62  $\text{g}/\text{cm}^3$ .

### 2.2 Metallographic and Mechanical Specimens' Preparation

All the metallographic and mechanical specimens in this work were prepared using the L-PBF technology. The L-PBF process was performed with an EOS M280 machine (EOS GmbH, Germany). The process was carried out in an argon atmosphere with the concentrations of  $\text{O}_2$  controlled under 1000 ppm. The linear raster scan with bi-directionally strategy was applied, and the orientation of the scanning track was rotated  $67^\circ$  after one layer of scanning. The substrate was preheated at a temperature of  $80^\circ\text{C}$ . The bulk specimens with dimensions of 8 mm  $\times$  8 mm  $\times$  8 mm were fabricated for the microstructure analysis and L-PBF parameters optimization. According to the L-PBF building direction of the specimen, the microstructure of the as-built specimen was analyzed along the direction of parallel and perpendicular to the scanning plane, as shown in Figure 2. The microstructure of the specimens was characterized by the scanning electron microscope (SEM, Hitachi S-4800) with an accelerated voltage of 15 Kv, electron backscattered diffraction (EBSD, FEIQUANTA FEG 650) and transmission electron microscope (TEM, FEI Tecnai 20) with the accelerated voltage of 200 kV.

The tensile specimens were built with the uniaxial tensile orientation parallel to the scanning plane. The L-PBF parameters were optimized according to the previous work of our research group (Ref 19). The laser power was 250 W, the

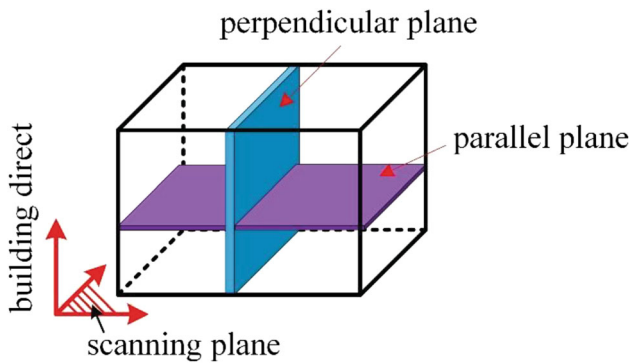


Fig. 2 Schematic diagram of scanning plane of the specimen

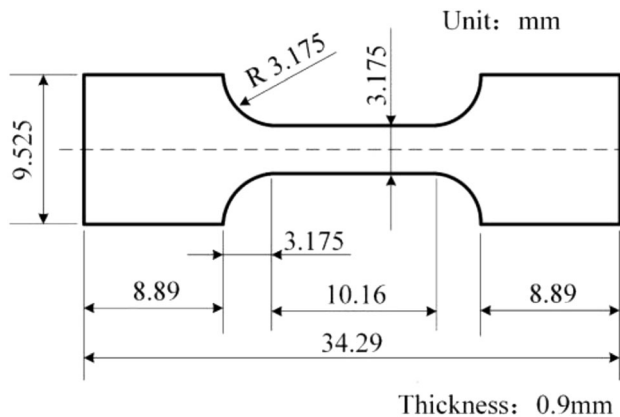


Fig. 3 Tensile specimens size diagram

scanning speed was 1100 mm/s and the hatching space was 0.09 mm. The mechanical properties were tested using INSTRON 5985 electronic universal material testing machine with a strain rate of 10<sup>-3</sup>/s. The tensile specimens were prepared using the optimum process parameters (LP 250 W, SS 1100 mm/s, HS 0.09 mm), and three specimens were measured for each specimen to ensure the accuracy of the experiments. The surfaces of the specimens were ground and polished with 200#, 400#, 600#, 800#, and 1000# sandpaper in that order. The tensile specimens were built with the uniaxial tensile orientation parallel to the scanning plane, and the sizing diagram is shown in Figure 3. The results were compared with those of as-cast alloys. Tensile test specimens were prepared with the optimum parameters, and the tensile specimens were built with the uniaxial tensile orientation parallel to the scanning plane.

### 2.3 Heat Treatment Process

To improve the mechanical properties of the as-printed specimens, three heat treatment regime of annealing, solid solution plus aging, and recrystallizing were designed according to the Cu-Sn phase diagram (Ref 21). The heat treatments were carried out in a high-temperature tube furnace with vacuum condition. The parameters of these heat treatments are shown in Table 1.

## 3. Results

### 3.1 Microstructure and Properties of the As-built Cu-10Sn Alloy

Figure 4 shows the microstructures of Cu-10Sn specimens fabricated by L-PBF. There are several pores in the specimen. As shown in Figure 4(a), the typical L-PBF characteristics of multiple melting point trajectories overlap are clearly shown on the horizontal plane that is parallel to the scanning surface. The melted scan tracks show a melting pool in an ellipse shape with irregular size, and the orientation of the major axis is generally along the direction of the scanning track. The brightly colored particles and a small number of pores are distributed along the edge of the ellipse curve. Figure 4(b) shows the microstructure of the specimen perpendicular to the scanning direction. With the action of the laser layer by layer, a fish-scale pattern laser action zone is finally formed. The fish-scale patterns area of each columnar grain is about 10 μm in width and 40 μm in length. The top and side views establish an assembly of SEM images on three perpendicular planes of the as-built Cu-10Sn specimens as shown in Figure 4(c). Each of the ellipses on the top view contains multiple grains. In the side view, the melting pool in a sector shape is oriented normal to the temperature gradient.

To further analyze the microstructure of the as-built Cu-10Sn alloy, the alloy was analyzed using TEM. Figure 5 shows the TEM image of the local region of the as-built Cu-10Sn alloy. The subgrain exists in the Cu-10Sn alloy with a length of about 100 nm and a width of about 100 nm. There are high-density dislocations in the subgrain, and the high-density dislocations are entangled directly to each other.

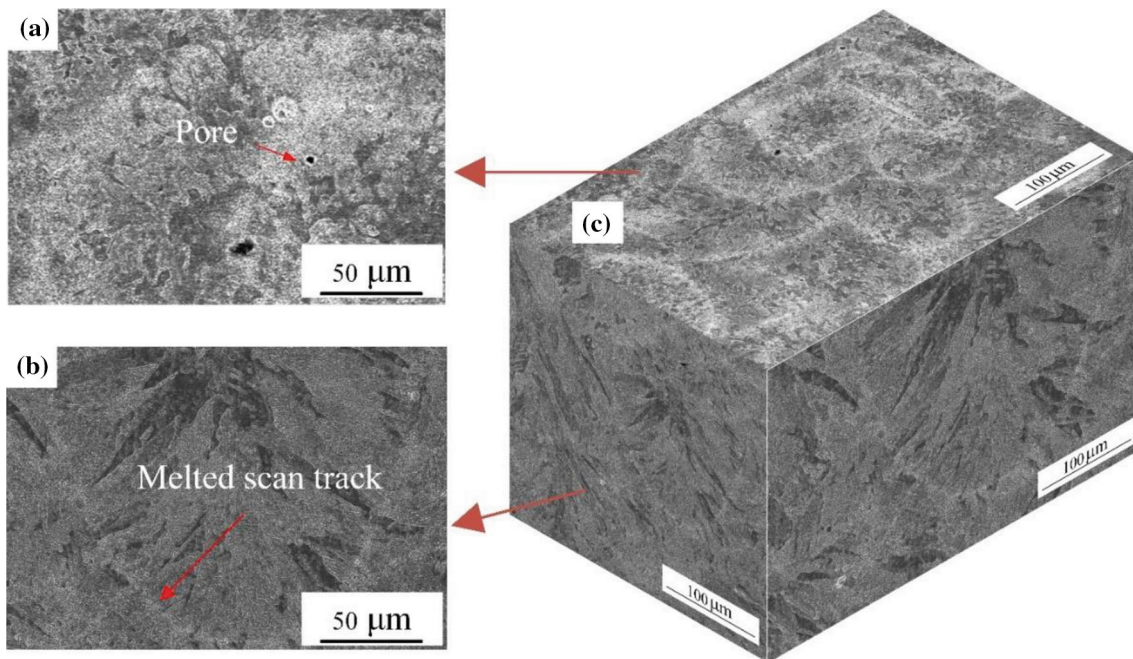
### 3.2 Microstructure Evolution of the As-built Cu-10Sn Alloy After Heat Treatment

Figure 6 shows the microstructure and the grain size of the specimen after different heat treatments. Compared with the as-built specimens, the HT-1 specimen after the annealing treatment keeps the original microstructure, as presented in Figure 6(a), due to the low heat treatment temperature. Although some of the defects and surface defects disappear in the recovery stage, the grain size and most of the defects remain intact. The microstructure of the HT-3 specimen after the recrystallization treatment is quite different from that of the HT-1 specimen, as shown in Figure 6(c). First of all, coarsening of grains after HT-3 treatment, and there are twin structures in some grains. In the process of grain growth, pores tend to gather and distribute in the grain boundary region. In this case, the microstructure of the specimen that parallels to the scanning plane is almost the same as that of the specimen perpendicular to the scanning plane. After the HT-2 treatment as presented in Figure 6(b), the grains in the HT-2 specimens are transformed into the equiaxed grains. No clear crystallographic orientation is seen in the IPF diagram of Figure 6(a1, b1, c1). The grain size is statistically calculated from these IPF microstructure images, as shown in Figure 6(a2, b2, c2). After the annealing treatment, the grain size does not change significantly. After the recrystallization treatment, the grain size grows significantly and has a grain area distribution across several orders of magnitude. After HT-2 treatment, there are still fine grains in the specimen.

**Table 1 Heat treatment conditions for the as-built Cu-10Sn specimen**

Batch number	Treatment type	Heat treatment process
HT-1	Annealing	340°C/2 h/ Air cooling (AC)
HT-2	Solution and aging treatment	800°C/2 h/AC + 400°C/4 h/AC
HT-3	Recrystallization	860°C/1 h/AC

AC:short for Air cooling.



**Fig. 4** Microstructure of the as-built Cu-10Sn alloy: (a) parallel to the scanning plane; (b) perpendicular to the scanning plane; (c) an assembly of SEM images (secondary electron image) on three perpendicular planes

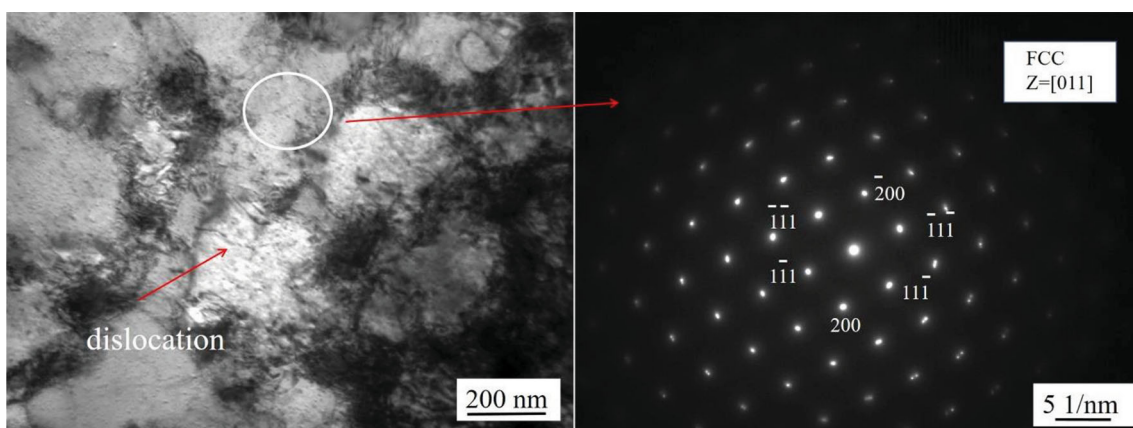


**Fig. 5** TEM image of as-printed L-PBF Cu-10Sn alloy

Figure 7 shows the TEM diagrams of the Cu-10Sn alloy specimens with different heat treatments. Compared to Figure 5 and 7, the HT-1 specimen with the annealing treatment possesses fewer dislocations. The growth of the subgrain can be seen from the microstructure images, which comes from the rearrangement of dislocation movement during the HT-1 treatment. As shown from the dark field TEM image of the

HT-3 specimen with the recrystallization treatment, the twin structure is generated in the microstructure of the alloy with the recrystallization treatment. In some areas, the phenomenon of the dislocation disentanglement can still be observed. The nucleation of the twins could be promoted by the accumulations of dislocations and stresses. After the solution and aging

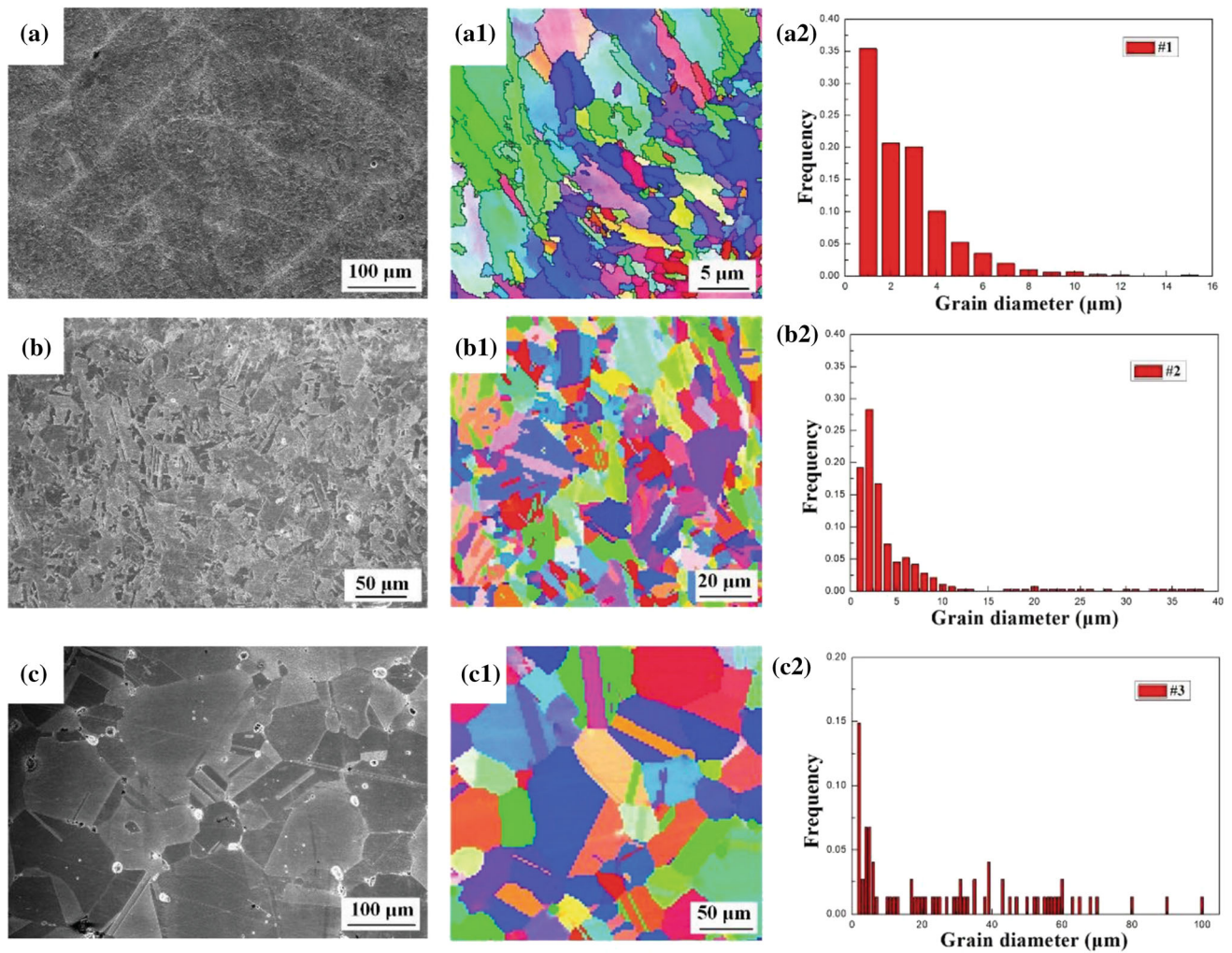


**Fig. 6** Microstructure and grain size of the Cu-10Sn specimen with different heat treatments: (a, a1, a2) HT-1 treatment; (b, b1, b2) HT-2 treatment; (c, c1, c2) HT-3 treatment; (a, b, c) SEM images of the different heat treatments specimens; (a1, b1, c1) EBSD analysis of the different heat treatments specimens; (a2, b2, c2) The grain size after different heat treatments

treatment, the twin structure exists in the microstructure of the HT-2 specimen.

### 3.3 Mechanical Properties of the As-built Cu-10Sn Alloy After Heat Treatment

Figure 8 shows the true stress–strain curve of the specimens in a quasi-static tensile experiment. Compared with the casted Cu-10Sn specimen, the yield strength ( $\sigma_{0.2}$ ), the UTS and elongation of the L-PBF fabricated specimens are greatly improved. The quasi-static tensile yield strength ( $\sigma_{0.2}$ ) and the UTS of the Cu-10Sn specimen increase from 130 MPa and 230 MPa (casted specimens) to 392 MPa and 749 MPa (as-built specimens). Similarly, the elongation of the material increased around 11-29% from the casted specimen to the as-built specimen. Compared with the original specimens, the yield strength decreases with the heat treatments, but the tensile strength and elongation increase significantly after HT-1 and HT-2 treatment. After the HT-2 treatment, the (UTS) and elongation of the specimens increase to 840 MPa and 56%, respectively, which is the highest in all these heat treatment processes.

## 4. Discussion

Figure 4 shows the microstructures of Cu-10Sn specimens fabricated by L-PBF. A distinct layered microstructure is observed in the vertical plane, which is built by the overlap of the melt channel with both boundary (Ref 22). A fine arrangement of the fish-scale patterns regions can be observed. Columnar grains, as the typical grain morphology of L-PBF, are usually fabricated through epitaxial growth due to the remelting of the previous depositing layer and the significant temperature gradient between the depositing layers (Ref 23). When the laser scans on the surface of the specimen, the temperature attenuates from the center to the surrounding, and the temperature gradient is large. The microstructure grows along the temperature gradient, which leads to the forming of columnar grain. With the action of the laser layer by layer, a fish-scale pattern laser action zone is finally formed. The growth direction is parallel to the temperature gradient. Due to the temperature gradient between the melted layer and the solidified layer, the growth direction of the columnar grain is parallel to the temperature gradient. The column grains growing

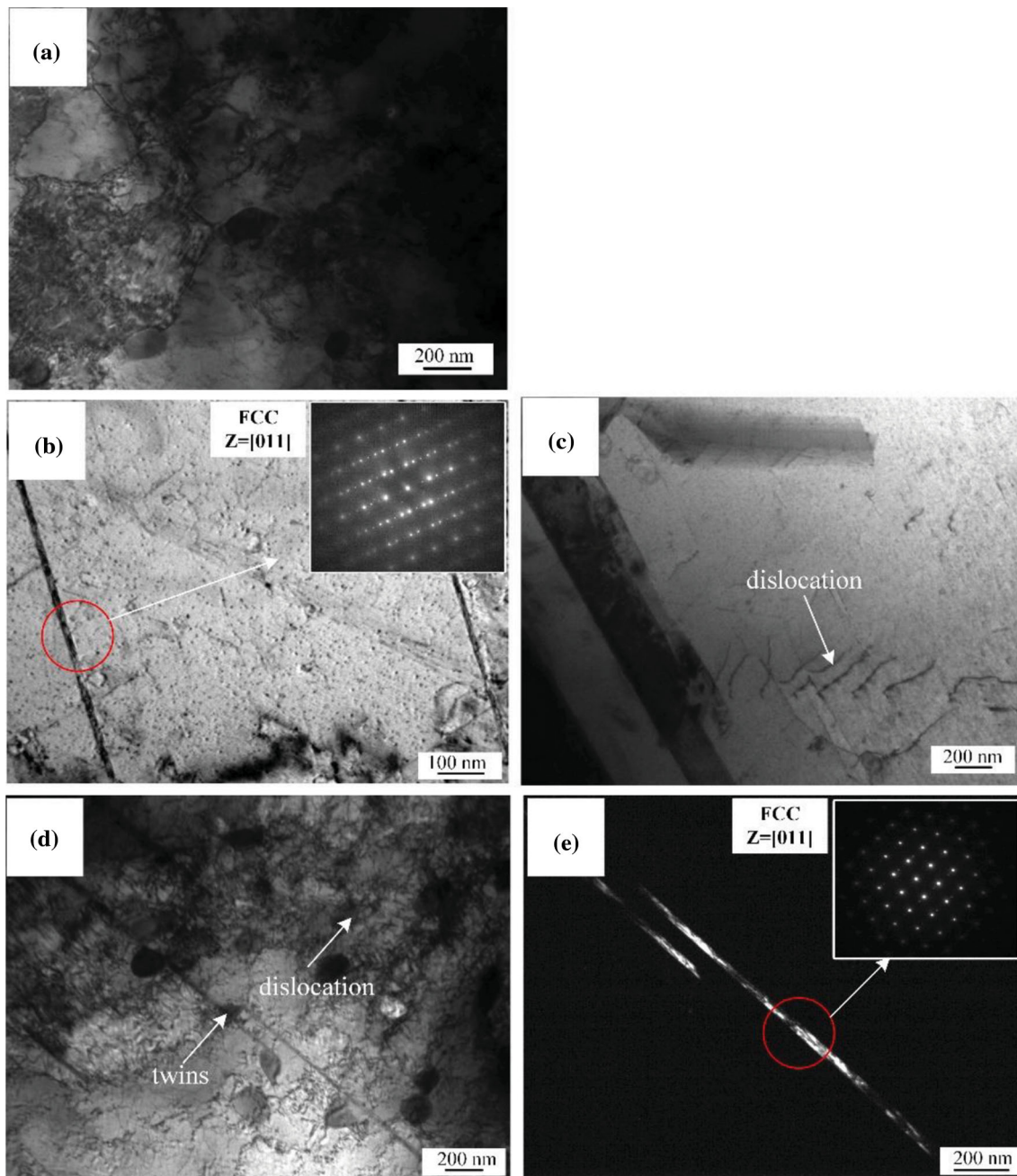


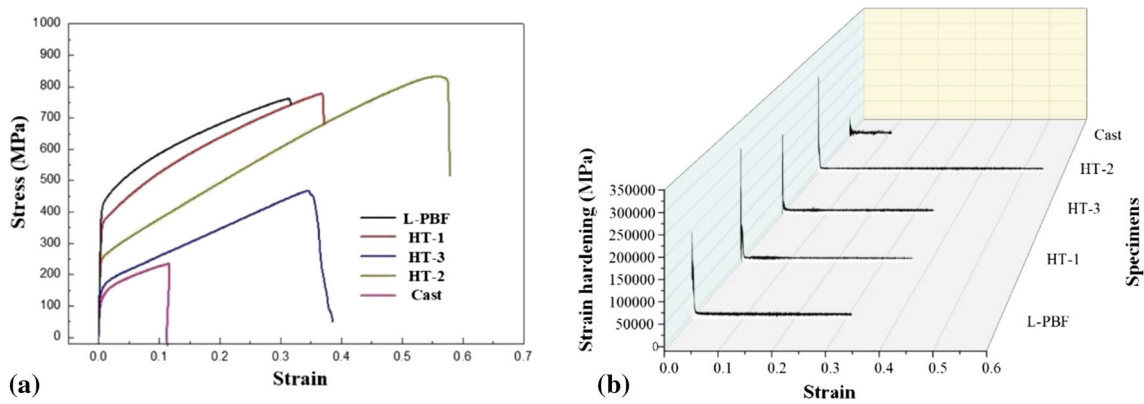
**Fig. 7** TEM image of the as-built Cu-10Sn specimen with different heat treatments: (a) the HT-1 treatment; (b, c) the HT-2 treatment; (d, e) the HT-3 treatment

along the building direction are favored by the direction of heat transfer during the L-PBF process (Ref 24, 25).

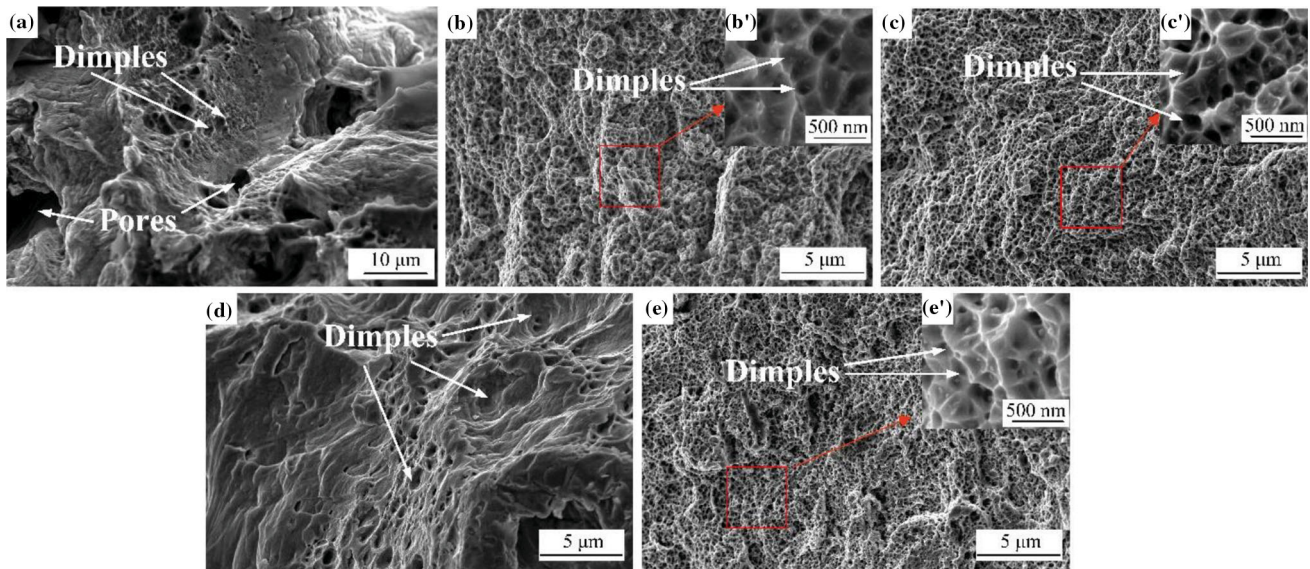
According to the electron diffraction information ( $2\theta=76.02^\circ$ ,  $d\text{-Spacing}=0.1259\text{ nm}$ ,  $\{hkl\}=\{200\}$ ), as shown in Figure 5, it indicates the face center cubic (FCC) structure is  $\alpha\text{-Cu}$ . The  $\alpha\text{-Cu}$  structure prevails through all the surfaces, so their compositions were uniform. There are high-density dislocations in the subgrain, and the high-density dislocations are entangled directly to each other. These dislocations could be generated during the rapid cooling process of the melting pool during the L-PBF process (Ref 26).

Figure 6 shows the microstructure and the grain size of the specimen after different heat treatments. Because copper alloy belongs to the FCC structure and the stacking fault energy is

low (Ref 27), twins tend to form in the process of heat treatment. And the HT-2 treatment also occurred at a higher temperature. The dendrite formed by rapid cooling gradually changed into an equiaxed grains structure through atomic diffusion. However, because the temperature is slightly lower than that in the recrystallization treatment of the HT-3 specimen, there is no large-scale grain growth spotted. The color and morphology variation within different grains suggests slight variations of crystallographic orientation among the constituent subgrains. However, no clear crystallographic orientation is seen in the IPF diagram of Figure 6(a1, b1, c1). The grain size is statistically calculated from these IPF microstructure images, as shown in Figure 6(a2, b2, c2). After the annealing treatment, and the grain size does not change



**Fig. 8** Mechanical properties images; (a) the true stress–strain curves in the quasi-static tensile experiments for the specimens; (b) the strain hardening behaviors of the specimen as a function of true strain



**Fig. 9** SEM images (secondary electron images) of the fracture surfaces after quasi-static tensile test; (a) Casting; (b) As-built; (c) the HT-1 treatment; (d) the HT-3 treatment; (e) the HT-2 treatment; (b', c', e') Magnification micrograph of the selected square region in (b, c, e)

significantly, so it keeps high strength. After the recrystallization treatment, the grain size grows significantly and has a grain area distribution across several orders of magnitude leading to a reduction in the strength of the material. After HT-2 treatment, there are still fine grains in the specimen, but it can be seen that the specimen transforms into equiaxed grains resulting in good mechanical properties.

Figure 8a shows the true stress–strain curve of the specimens in a quasi-static tensile experiment. Compared with the casted Cu-10Sn specimen, the yield strength ( $\sigma_{0.2}$ ), the UTS and elongation of the L-PBF fabricated specimens are greatly improved. This is attributed to the extremely fine grain and the dislocations in the as-built specimens due to the high cooling rate in the L-PBF processing, which proves the effectiveness of L-PBF to improve the mechanical properties of the materials. Firstly, the grains of as-built specimens are much finer than that of the as-cast specimens (Ref 13). This apparent fine grain strengthening can significantly increase the strength of the specimen. Second, the further movement and proliferation of the dislocations are hindered, which increases the strength of

the Cu-10Sn alloy specimens (Ref 28). As a result, grain refinement and the formation of a large number of dislocations are the main reasons for the high strength of the L-PBF specimens. Compared with the original specimens, the yield strength decreases with the heat treatments, but the tensile strength and elongation increase significantly after HT-1 and HT-2 treatment. After the HT-2 treatment, the (UTS) and elongation of the specimens increase to 840 MPa and 56%, respectively, which is the highest in all these heat treatment processes. Figure 8b shows the strain hardening behaviors of the specimen as a function of true strain. The strain hardening rate of the alloy decreases sharply at the beginning of plastic deformation and then plateaus with further increases in strain. The graph shows that the HT-2 treated ones have a higher strain hardening capacity throughout the plastic deformation process, indicating a better capacity for uniform plastic deformation. This is due to the formation of finer grains within the HT-2 treated specimen.

The mechanical properties in the tensile test are mainly related to the microstructure of the materials, while dislocation

strengthening and grain size strengthening play a dominant role. The increase in UTS and elongation is mainly due to the interaction between small twins and dislocation. The reduction in yield strength is because of the growth of the grain size and the reducing of the dislocation after heat treatment (Ref 20). The grain size of specimens increased after HT-3 treatment, so the yield strength is lower than the other specimens. As shown in Figure 7, a large number of dislocations are generated near the twin boundary after the solution and aging treatment. According to Gregg's work, the accumulation of the dislocation near the twin increases the strength of the specimens and the plasticity of the materials, which explains the enhancing of the mechanical properties for the HT-2 specimen (Ref 28). A large number of dislocations are formed on the boundary of the twin after the solution and aging treatment, which lead to work hardening and coordinate plastic deformation (improve toughness) (Ref 29). The introduction of smaller-scale twins can strengthen the metal material and improve the plasticity at the same time.

Figure 9 shows SEM images of the tensile fracture morphology of specimens after tensile tests, respectively. The number of dimples in the as-cast Cu-10Sn alloy specimens was low. As shown in Figure 9(a), only some of the fracture surfaces had dimples. Compared to the tensile fractures of the conventional cast Cu-10Sn alloy, the size of ductile dimples was much smaller than those obtained in as-cast and the number of dimples is significantly higher than in as-cast. A great number of dimples with small size indicated more surface energy produced during the fracture process, which reflected higher strength (Ref 30). In addition, the size of dimples depended to a great extent on the size of subgrains (Ref 31). As shown in Figure 9b' (magnification of the rectangular area in Figure 9b), the average dimple size was approximate 300nm. Figure 9(c-e) shows the fracture morphology after different heat treatments, respectively, and the specimens also exhibit ductile fracture. As shown in Figure 9(c', e') (a magnification of the rectangular area in Figure 9(c, e)), the average dimple size was approximately 300nm. However, after the recrystallization treatment, the dimples of the specimens were significantly reduced, and the grain size of the specimens became larger. This is also the reason for the decrease in strength (Ref 30).

## 5. Conclusions

In this paper, the microstructure and mechanical properties of the as-built Cu-10Sn specimens with different heat treatments have been investigated. The following conclusions can be obtained.

1. The grain shape of the as-built Cu-10Sn alloy is mainly a columnar shape built along the temperature gradient. The strength and plasticity of the as-built specimen are much higher than that of the casted Cu-10Sn alloy, mainly because of the grain refinement in the grain of the as-built specimen.
2. The microstructure of the specimen has different microstructural characteristics at different heat treatment temperatures. After HT-2 treatment, the grains in the specimens are transformed into the equiaxed grains. The equiaxed and twinned structures in the grains can improve their UTS and EL properties.

## Acknowledgment

The authors would like to thank the financial support for this work from the General Program of Science and Technology Development Project of Beijing Municipal Education Commission (KM202010005006).

## References

1. J. Park, C. Park and K. Lee, Implication of Peritectic Composition in Historical High-Tin Bronze Metallurgy, *Mater. Charact.*, 2009, **60**, p 1268–1275.
2. A. Tavakoli, R. Liu and X.J. Wu, Improved Mechanical and Tribological Properties of Tin–Bronze Journal Bearing Materials with Newly Developed Triballoy Alloy Additive, *Mater. Sci. Eng. A.*, 2008, **489**, p 389–402.
3. X.H. Chen, Z.D. Wang, D. Ding, H. Tang, L.L. Qiu, X. Luo and G.D. Shi, Strengthening and Toughening Strategies for Tin Bronze Alloy Through Fabricating In-Situ Nanostructured Grains, *Mater. Des.*, 2015, **66**, p 60–66.
4. X. Li, T. Ivas, S.A.B. Spierings, K. Wegener and C. Leinbach, Phase and Microstructure Formation In Rapidly Solidified Cu-Sn and Cu-Sn-Ti Alloys, *J Alloy Compd*, 2018, **35**, p 1374–1382.
5. X. Zhao, Q.S. Wei, B. Song, Y. Liu, X.W. Luo, S.F. Wen and Y.S. Shi, Fabrication and Characterization of AISI 420 Stainless Steel Using Selective Laser Melting, *Mater. Manuf. Process.*, 2015, **30**, p 1283–1289.
6. I. Yadroitsev and I. Smurov, Selective Laser Melting Technology: from the Single Laser Melted Track Stability to 3D Parts of Complex Shape, *Phys. Procedia.*, 2010, **5**, p 551–560.
7. D.D. Gu, W. Meiners, K. Wissenbach and R. Poprawe, Laser Additive Manufacturing of Metallic Components: Materials, Processes and Mechanisms, *Int. Mater.*, 2013, **57**, p 133–164.
8. L. Thijs, F. Verhaeghe, T. Craeghs, J.V. Humbeeck and J.P. Kruth, A Study of the Microstructural Evolution During Selective Laser Melting of Ti–6Al–4V, *Acta Mater.*, 2010, **8**, p 3303–3312.
9. T. Gustmann, A. Neves and U. Kühn, Influence of Processing Parameters on the Fabrication of a Cu-Al-Ni-Mn Shape-Memory Alloy by Selective Laser Melting, *Addit. Manuf.*, 2016, **11**, p 23–31.
10. G.M. Zhang, C. Chen, X.J. Wang, P.W. Wang, X.Y. Zang, X.P. Gan and K.C. Zhou, Additive Manufacturing of Fine-Structured Copper Alloy By Selective Laser Melting of Pre-Alloyed Cu-15Ni-8Sn Powder, *Int. J. Adv. Manuf. Tech.*, 2018, **6**, p 4223–4230.
11. D.H. Dai and D.D. Gu, Thermal Behavior and Densification Mechanism During Selective Laser Melting of Copper Matrix Composites: Simulation and Experiments, *Mater. Des.*, 2014, **55**, p 482–491.
12. D.C. Walker, W.F. Caley and M. Brochu, Selective Laser Sintering of Composite Copper–Tin Powders, *J. Mater. Res.*, 2014, **29**, p 1997–2005.
13. S. Scudino, C. Unterdörfer and K.G. Prashanth, Additive Manufacturing of Cu–10Sn Bronze, *Mater. Lett.*, 2015, **56**, p 202–204.
14. Y. Karabulut, E. Tascioglu, Y. Kayna, Heat Treatment Temperature-Induced Microstructure, Microhardness and Wear Resistance of Inconel 718 Produced by Selective Laser Melting Additive Manufacturing, *Optik*, 2019.
15. S. Raghavan, B.C. Zhang, P. Wang, C.N. Sun, M.L. Nai, T. Li and J. Wei, Effect of Different Heat Treatments on the Microstructure and Mechanical Properties in Selective Laser Melted INCONEL 718 Alloy, *Mater. Manuf. Process.*, 2017, **32**, p 1588–1595.
16. D.C. Tsai, M.J. Deng, Z.C. Chang, B.H. Kuo, E.C. Chen, S.Y. Chang and F.S. Shieu, Oxidation Resistance and Characterization of (AlCrMoTaTi)-Six-N Coating Deposited via Magnetron Sputtering, *J. Alloy. Compd.*, 2015, **647**, p 179–188.
17. H. Chen, A. Kauffmann, B. Gorr, D. Schliephake, C. Seemüller and J.N. Wagner, Microstructure and Mechanical Properties at Elevated Temperatures of a New Al-Containing Refractory High-Entropy Alloy Nb-Mo-Cr-Ti-Al, *J. Alloy. Compd.*, 2016, **661**, p 206–215.
18. Z. Mao, D. Zhang and P. Wei, Manufacturing Feasibility and Forming Properties of Cu-4Sn in Selective Laser Melting, *Materials.*, 2017, **10**, p 333.
19. Z. Tan, X.Y. Zhang, Z.L. Zhou, Z. Zhou, Y. Yang, X.Y. Guo, Z.J. Wang, X. Wu, G.H. Wang and D.Y. He, Thermal Effect on the



- Microstructure of the Lattice Structure Cu-10Sn Alloy Fabricated Through Selective Laser Melting, *J. Alloy. Compd.*, 2019, **787**, p 903–908.
20. A.P. Ventura, C.A. Wade and G. Pawlikowski, Mechanical properties and Microstructural Characterization of Cu-4.3 Pct Sn Fabricated By Selective Laser Melting, *Metall. Mater. Trans. A.*, 2016, **48**, p 1–10.
  21. N. Saunders and A.P. Miodownik, The Cu-Sn (Copper-Tin) System, *Alloy. Phase. Diagr.*, 1990, **11**, p 278–287.
  22. B. AlMangour and J.M. Yang, Understanding the Deformation Behavior of 17–4 Precipitate Hardenable Stainless Steel Produced By Direct Metal Laser Sintering Using Micropillar Compression and TEM, *Int. J. Adv. Manuf. Technol.*, 2017, **90**, p 119–126.
  23. H. Zhang, H.H. Zhu, T. Qi, Z.H. Hu and Z.Y. Zeng, Selective Laser Melting of High Strength Al-Cu-Mg alloys: Processing, Microstructure and Mechanical Properties, *Mater. Sci. Eng. A.*, 2016, **656**, p 47–54.
  24. A. Popovich, V. Sufiarov, I. Polozovn, E. Borisov, D. Masaylo and A. Orlov, Microstructure and Mechanical Properties of Additive Manufactured Copper Alloy, *Mater. Lett.*, 2016, **17**, p 938–941.
  25. K. Kunze, T. Etter, J. Grässlin and V. Shklover, Texture, Anisotropy in Microstructure and Mechanical Properties of IN738LC Alloy Processed by Selective Laser Melting (SLM), *Mater. Sci. Eng. A.*, 2014, **620**, p 213–222.
  26. M. Balbaa, S. Mekhiel, M. Elbestawi and J. Mclsaac, On Selective Laser Melting of Inconel 718: Densification, Surface Roughness, and Residual Stresses, *Mater. Des.*, 2020, **193**, p 1–22.
  27. I. Maskery, N.T. Aboulkhair and A.O. Aremu, A Mechanical Property Evaluation of Graded Density Al-Si10-Mg Lattice Structures Manufactured by Selective Laser Melting, *Mater. Sci. Eng. A.*, 2016, **670**, p 264–274.
  28. J. Gregg and W. Soffa, Preliminary Observations of the Flow and Fracture of Copper-Titanium Alloy Single Crystals Containing Coherent Precipitates, *Scripta Metal.*, 1978, **12**, p 525–529.
  29. Y. Zhang, Y.S. Li, N.R. Tao and K. Lu, High Strength and High Electrical Conductivity in Bulk Nanograined Cu Embedded with Nanoscale Twins, *Appl. Phys. Lett.*, 2007, **91**, p 282–285.
  30. H.L. Yao, T. Zhen, D.Y. He, Z.L. Zhou, Z. Zhou, Y.F. Xue, L. Cui, L.J. Chen, G.H. Wang and Y. Yang, High Strength and Ductility AlCrFeNiV High Entropy Alloy with Hierarchically Heterogeneous Microstructure Prepared by Selective Laser Melting, *J. Alloy. Compd.*, 2020, **813**, p 152196–152196.
  31. Y. Zhong, L. Liu, S. Wikman, D. Cui and Z. Shen, Intragranular Cellular Segregation Network Structure Strengthening 316L Stainless Steel Prepared by Selective Laser Melting, *J. Nucl. Mater.*, 2016, **470**, p 170–178.

**Publisher's Note** Springer Nature remains neutral with regard to jurisdictional claims in published maps and institutional affiliations.